Modelling powder compaction with consideration of a deep grooved punch

G. Alonso Aruffo, Mohammed Michrafy, Driss Oulahna, Abderrahim Michrafy

Modelling powder compaction with consideration of a deep grooved punch

G. Alonso Aruffo [a,*], M. Michrafy [b], D. Oulahna [a], A. Michrafy [a]

[a] Université de Toulouse, IMT Mines Albi, CNRS, Centre RAPSODEE, 81000 Albi, France
[b] Kedge Business School, 680 cours de la Libération, 33405 Talence, France

Keywords:
Finite element modelling
DPC hybrid calibration
Parallelepiped grooved compact
X-ray tomography

A B S T R A C T

In this work a modelling approach for predicting density distribution in the vicinity of two facing grooves on a parallelepiped compact surface, is developed and results are validated using X-ray tomography. An experimental hybrid procedure is proposed to calibrate Drucker-Prager Cap model material parameters which are numerically validated and considered for FEM compaction simulation of grooved specimen using Arbitrary Lagrangian Eulerian method (ALE). Results of the predicted density show high values under the groove and low values on its flanks and shoulders. Similar findings were observed in the literature. Additionally, a strong density gradient between the facing grooves is predicted and validated, demonstrating that the calibrated model achieved good agreements with the measurements.

The proposed hybrid calibration procedure could be used for other shape and size die not benefiting from radial instrumentation. Moreover, the ALE approach demonstrated its robustness in solving die powder compaction in presence of strong mesh distortions.

1. Introduction

Powder die compaction is a widely used manufacturing process either for ceramic, metallic or pharmaceutical powders [1]. This forming process is particularly useful for the production of complex shaped compacts. However, the final shape and relative density gradients in the compact are, among others, dependent on the complex geometry of the punches used, their loading motion [2] and wall friction [3]. Understanding of the development of stress and relative density fields in compaction process is thus a crucial step for improving product quality.

In pharmaceutical applications, various experimental and numerical studies have examined the impact of the punch shape surface on the relative density distribution. Some of them were particularly conducted on concave or convex punch surfaces [4–8,10,12]. In their study, Eiliazadeh et al. [4] investigated the axial and radial movement of powder and the density distribution using a coloured layer technique and digital image analysis. Results showed that the tablets produced were highly non-homogeneous with high density regions in the "top corners" adjacent to the moving punch surface. In the work of Sinka et al. [5], the non-destructive technique based on X-ray tomography was developed to measure density distribution of capsule shape tablets. They showed high relative density values in the valley of the singularity and low values on the shoulders demonstrating the complexity of the material flow in the "died corners". Later, Djemai et al. [6] investigated the effect of wall friction and tablet shape on the density distribution using the nuclear magnetic resonance technique for 3D mapping of the relative density distribution. This method, which does not require special calibration, as the signal is directly proportional to the porosity for the imaging conditions used, was validated by direct comparison with X-ray computed tomography. The results clearly showed the effect of wall friction on density distribution by curved faced tablets using clean and pre-lubricated tooling. Using experimental and finite element modelling (FEM), Wu et al. [7], Han et al. [8] and Kadiri et al. [10] examined the effect of convex punch shape on relative density distribution and showed that the FE modelling of the density and stress distribution could be used to analyse and explain the capping and lamination tendency. Krock et al. [12] examined numerically the influence of friction on the compaction process for the flat-face, flat-face radius edge, and standard convex tablets highlighting the effects of friction change on the tablet shape. Analysing the impact of three punch shapes used in industrial standards, Diarra et al. [13] showed that, flat and convex tablets, even obtained with the same compaction force, do not have the same density at the centre of the compact furthermore, the tablets presented differences in their tensile strength. Again, this result revealed the large variation of density in tablets compacted with the deepest punch.

* Corresponding author.
E-mail address: gweni.alonso_aruffo@mines-albi.fr (G. Alonso Aruffo).

Other studies were dedicated to the effect of embossed punch features on tablet compaction and density distribution [9,11,14]. Han et al. [9] compared results from 2D-SAXS (small-angle X-ray scattering) with FE simulations of compacts with complex shapes, including cylindrical flat-faced punch and shaped lower punch with different central protrusions. Variation in compaction behaviour were observed due to friction against the die walls and the punch shape. Laity [11] studied the effect of embossed punch features on the compaction behaviour of cylindrical tablets manufactured with single or double furrows across the tablet surface. Results of relative density showed higher values at the furrow base and smaller ones near the furrow's flanks. The case of double furrows showed smaller density regions around the furrows, which were prone to cracking and flanking. In their study of modelling the formation of debossed features on a pharmaceutical tablet, Swaminathan et al. [14] investigated by FE modelling and X-ray tomography the relative density distribution in the vicinity of a debossed feature defined by five geometrical parameters. A parametric study on the compaction behaviour was also proposed. Both measurements and numerical predictions showed the smallest relative density values at the shoulders of the debossed feature and the largest values at the base of the valley.

Regarding the FE simulation of debossed tablets in [9,14], the authors considered a modified density-dependent Drucker-Prager Cap (DPC) model, which was calibrated based on the standard calibration method [15]. The elastic material properties were also density-dependent. The FE simulation in [9] was conducted in 2D on cylindrical compacts of 10 mm of diameter and 4.92 and 5.54 mm of height. Cylindrical, hemispherical and conical protrusion singularities were considered at lower punch and the compaction was done with a flat punch on the powder top. The simulation used an implicit procedure in Abaqus/Standard and mesh to mesh solution mapping. Opposite to this, the simulation method in [14] was based on the explicit method in Abaqus/Explicit using an adaptive mesh algorithm. The simulation was conducted in 2D on cylindrical compact of 3.5 mm of diameter and 1.46 mm of height. The upper punch with embossed part of 0.29 mm of stroke width and 0.18 mm of stroke depth indented the powder during the compaction. The impact of parameters describing the singularity shape on relative density distribution was also investigated. In these studies, the size and shape of the simulated compacts was similar to the compacts that were used to calibrate the DPC parameters.

The present work focuses on the compaction behaviour of powder using a parallelepiped die with large dimensions ($x = 1.56$ cm, $y = 5.4$ cm and $z = 4.0$ cm) and two facing punches with grooved parts

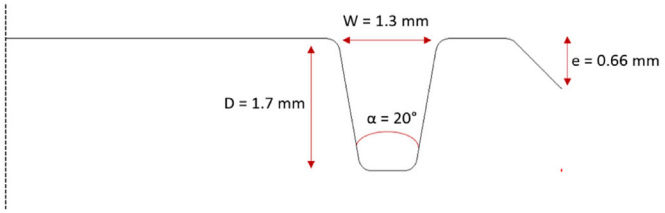

Fig. 2. Geometrical characteristics of grooved punch surface (due to the symmetry, only one groove is showed).

and chamfers (Figs. 1, 2). This configuration has not been studied yet due to the die shape, punch surface and powder height, which requires the simulation of large strain making the implicit computation, commonly used for die compaction simulations, inefficient. An alternative was to develop FE simulations using the ALE explicit method in Abaqus/Explicit. This method is generally recommended for solving problems of large distortions as in the rolling compaction process [16–20]. Regarding material parameters calibration of the DPC model, a hybrid calibration procedure is proposed as the parallelepiped die does not benefit from radial instrumentation and DPC data of a cylindrical small compact [23,24] cannot be scaled for the simulation of the large parallelepiped compact. The obtained data was numerically validated and used for compaction simulation of the grooved specimen. The predicted relative density was validated based on measurements of X-ray tomography.

This paper is organized as follows: Section 2 describes the DPC model and the proposed hybrid procedure for the calibration of material parameters. Elastic behaviour is considered linear, isotropic and density-dependent. The methodology of its characterization is described. Finally, wall friction coefficient and the procedure of its determination is presented. Section 3 presents results of DPC material parameters of microcrystalline cellulose powder vivapur®102 (MCC), elastic properties and wall friction according to relative density. For this, compaction behaviour of MCC considered both tests in instrumented cylindrical die and parallelepiped die as described in the previous section. At end of this section, X-ray tomography characterization and mapped relative density are presented. Section 4 details finite element simulation of the compaction performed using the ALE explicit method. Then, numerical validation of DPC material parameters of MCC is presented in the case of flat punches. For the case study of the grooved compact, Von-Mises stress and relative density distributions of the grooved compact are presented and discussed. Thereafter,

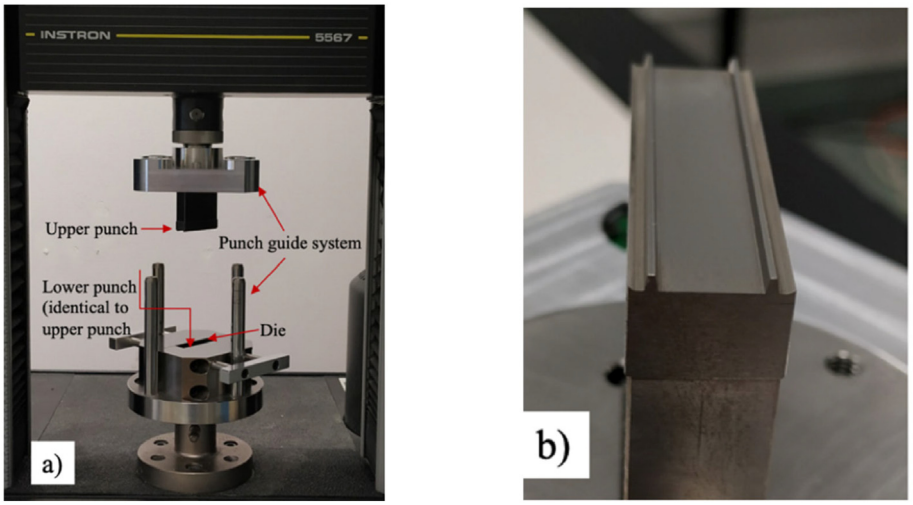

Fig. 1. Design of parallelepiped die compaction system, a) and grooved punch surface, b).

comparison of the predicted and measured relative density distributions using X-ray tomography is discussed. Section 5 summarizes the main conclusions.

2. Constitutive model and calibration

2.1. Drucker-Prager/cap model

The DPC model used herein is defined by three surfaces in pressure and Von-Mises stress space [21] (Fig. 3):

- A linear shear failure surface Fs which is expressed as:

$$q - p\tan\beta - d = 0 \tag{1}$$

Where: β is the material friction angle, d is the material cohesion, $p = \frac{1}{3} trace(\sigma)$ is the hydrostatic stress and $q = \sqrt{\frac{3}{2}(S:S)}$ is the module of the deviatoric stress or Von-Mises stress. The deviatoric stress is defined as:

$$S = \sigma - pI$$

where: σ is the stress tensor and I is the identity matrix.

- An elliptical cap surface Fc governing the material densification defined as

$$\sqrt{(p-p_a)^2 + \left[\frac{Rq}{1+\alpha-\alpha/\cos\beta}\right]^2} - R(d + p_a\tan\beta) = 0 \tag{2}$$

where: R is a material parameter controlling the eccentricity of the cap, α,is a transition surface radius usually lower than 0.05 and fixed to 0.03 in this work $\left(1+\alpha-\frac{\alpha}{\cos\beta} \cong 1\right)$. p_a is the hydrostatic pressure representing the abscissa value of the intersection of the cap and the shear surfaces (or transition surface F_t) (Fig. 3). Its value is calculated using Eq. (3):

$$p_a = \frac{p_b - Rd}{1 + R\tan\beta} \tag{3}$$

  - A transition surface connecting the shear surface Fs and the cap surface Fc with a smooth transition facilitating numerical computation.

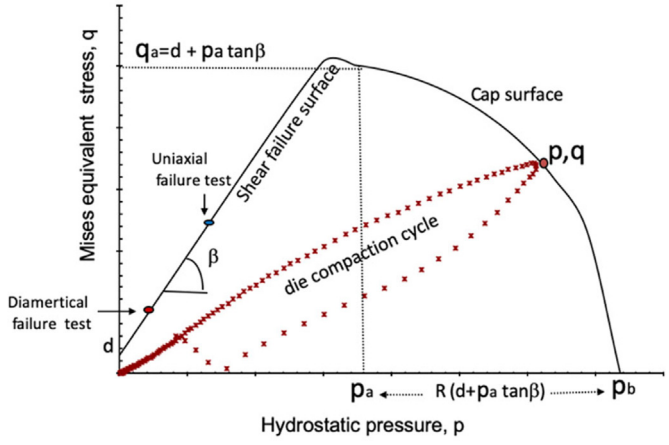

Fig. 3. DPC yield surfaces in hydrostatic pressure and Von Mises stress space. Three tests are required for parameters calibration: diametrical failure, axial failure and die compaction with radial stress measurement.

$$\sqrt{(p-p_a)^2 + \left[q - \left(1 - \frac{\alpha}{\cos\beta}\right)(d + p_a\tan\beta)\right]^2} - \alpha(d + p_a\tan\beta) = 0 \tag{4}$$

In the context of elastic-plastic modelling, the DPC model requires a hardening law of the cap surface determined by the relation of hydrostatic compression yield stress p_b, and the volumetric plastic strain ε_{vol}^{pl}, which is related to the material density as:

$$\varepsilon_{vol}^{pl} = \ln\left(\frac{\rho_0}{\rho_r}\right) \tag{5}$$

where ρ_0 is the initial relative density (loose material) and ρ_r is the current relative density.

For each relative density (or ε_{vol}^{pl}), within the region limited by the three yield surfaces, the material can be represented by an isotropic and elastic behaviour. However, when the stress state reaches the cap yield surface, the cap can expand as the volumetric plastic strain increases. This is the situation of the die compaction during loading. However, when the stress state reaches the shear failure surface (unloading), the material undergoes plastic volumetric increase (known as dilation mechanism) [22].

2.2. Hybrid procedure for DPC calibration

One of the difficulties of using the DPC model is the number and the complexity of the experiments required to calibrate its parameters. Five parameters are required: d and β for shear failure surface and p_a, R and p_b for the cap yield surface.

A standard procedure of calibration for cylindrical die compaction was proposed in [15]. The calibration of shear surface parameters (d, β) requires at least two tests with distinct failure stress states (i) a diametrical failure test and (ii) an axial failure test of cylindrical compacts. Both tests demand preparation of cylindrical compacts of different densities respecting the same experimental conditions (lubrication and aspect ratio of height to diameter of the compact). However, the calibration of p_a, R and p_b requires tests of die compaction and measurement of radial stress (or radial to axial stress ratio).

2.2.1. Calibration of cap surface (p_a, R and p_b)

Based on previous works [23,24], the hydrostatic pressure p_a, the cap eccentricity R and the hydrostatic yield pressure p_b are computed as:

$$p_a = \frac{-3q - 4d\ \tan\beta + \left(9q^2 + 24dq\tan\beta + 24pq\ \tan^2\beta + 16q^2\tan^2\beta\right)^{1/2}}{4\tan^2\beta} \tag{6}$$

$$R = \sqrt{\frac{2(p-p_a)}{3q}} \tag{7}$$

$$p_b = p_a + R(d + p_a\tan\beta) \tag{8}$$

Where: p and q are hydrostatic pressure and Von-Mises stress ((p, q) belongs to the cap surface (Fig. 3)) are computed from axial pressure σ_z and normal pressure, σ_r using instrumented cylindrical die [25]. Moreover, in die compaction, radial stress is often expressed using a proportional relationship in loading step ($\sigma_r = \gamma(\rho_r)\sigma_z$) and a linear relationship ($\sigma_r = a(\rho_r)\sigma_z + b(\rho_r)$) in the unloading [26]. These relationships were primarily proposed in [27] for a constant density.

In their study of compaction using a cubic die, Zhang et al. [28] considered a linear relationship between σ_z and normal stress σ_x (or σ_y) for the loading case where the ratio $\gamma = \frac{\sigma_x}{\sigma_z}$ was considered constant along z and x directions and independent of the geometry of the die wall. In the present work, using a parallelepiped die which was not instrumented,

the constants γ and a were determined from the axial stress/radial stress of loading unloading curve resulting from measurements of compaction cycle using instrumented cylindrical die. The measured, data which depend on the relative density, were considered for the compaction of the parallelepiped die as described below. Mainly, γ will be used to compute hydrostatic pressure and Von Mises stress (Eqs. (12) and (13)) from axial stress of the parallelepiped die compaction and a will be required to compute the elastic properties, Young Modulus and Poisson ratio (Eqs. (18) and (19)). The resulting DPC parameters and elastic properties will be numerically validated as described in the Section 4.

Based on the above considerations the normal stress on the parallelepiped die wall, can be expressed as:

For loading:

$$\sigma_x = \gamma\sigma_z \tag{9a}$$

For unloading:

$$\sigma_x = a\,\sigma_z + b \tag{9b}$$

Where: σ_z, is the axial pressure of the compaction using the parallelepiped die.

In the parallelepiped die compaction, hydrostatic pressure and Von Mises stress can be expressed as [28]:

$$p = \frac{1}{3}(\sigma_z + 2\sigma_x) \tag{10}$$

$$q = \frac{1}{2}\sqrt{(\sigma_y - \sigma_z)^2 + (\sigma_z - \sigma_x)^2} \tag{11}$$

Using Eq. (9a) in Eqs. (10) and (11), we obtain:

$$p = \frac{1}{3}\sigma_z(1 + 2\gamma) \tag{12}$$

$$q = \frac{\sigma_z}{\sqrt{2}}(1 - \gamma) \tag{13}$$

Eqs. (9a), (12) and (13) will be used for the calibration of material model parameters p_a, R and p_b using Eqs. (6), (7) and (8).

2.2.2. Calibration of shear surface (d,β)

Calibration of shear surface consists of the determination of the cohesion d and the internal friction angle β using diametrical failure and axial failure tests on cylindrical compacts. Because of the simplicity of the cylindrical geometry, d and β can be determined.

To characterize diametrical strength versus relative density, the diametrical failure force F_d of manufactured cylindrical compacts of MCC powder (Table 1) using lubricated die, was measured using the Erweka TBH30 apparatus. The strength was then computed using the Eq. (14).

$$\sigma_d = 2F_d/\pi DH \tag{14}$$

Where: D, is the compact diameter and H the compact height.

For axial strength characterization, compacts with an aspect ratio "height/diameter" ~2 was considered. For that, a set of compacts were manufactured using a lubricated die of 11.28 mm of diameter and 90 mm of height mounted on an Instron press equipped with a load force of 30 kN and a LVDT sensor for the displacement of the punch.

Table 1
Basic characteristics of powder MCC vivapur® 102.

Material	Average particle size (μm)	Bulk density (g/cm^3)	True density (g/cm^3)
MCC (vivapur® 102)	130	0.32	1.599 ± 0.0012

The mass was varied to obtain compacts with 22 mm of height. The resulting relative densities were in the range 0.4–0.9. The manufactured compacts were then subjected to an axial fracture test using the Instron press, paying attention to lubricate the punch and the support with magnesium stearate to reduce the barrel effect. Then, for each tablet the axial strength was computed from the axial strength force F_c using Eq. (15).

$$\sigma_c = 4F_c/\pi D^2 \tag{15}$$

In the above equation, D is the compact diameter.

The cohesion, d and internal friction angle, β were computed using Eqs. (16) and (17) [8,23].

$$d = \frac{\sigma_c\sigma_d}{\sigma_c + 2\sigma_d}\left(\sqrt{13} - 2\right) \tag{16}$$

$$\beta = tan^{-1}\left[\frac{3(\sigma_c + d)}{\sigma_c}\right] \tag{17}$$

From the measured diametrical and axial strength (Eqs. (14) and (15)), the cohesion and internal friction angle can be computed using Eqs. (16) and (17) as a function of relative density.

2.3. Elastic properties

The elastic behaviour of the material is considered linear, isotropic and density-dependent. In the parallelepiped die compaction, elastic properties (Young modulus, E and Poisson ratio, ν) were expressed as functions of bulk modulus and shear modulus leading to the following equations [23,28].

$$\frac{d\sigma_x}{d\sigma_z} = \frac{\nu}{1 - \nu} \tag{18}$$

$$\frac{d\sigma_z}{d\varepsilon_z} = \frac{E(1 - \nu)}{(1 + \nu)(1 - 2\nu)} \tag{19}$$

Where: $\frac{d\sigma_z}{d\varepsilon_z}$ is the slope of the unloading curve (ε_z, σ_z) of the compaction using the parallelepiped die and $\frac{d\sigma_x}{d\sigma_z} = a$, is the slope of the axial stress/radial stress of unloading (instrumented cylindrical die).

Consequently, the Poisson ratio is computed using Eqs. (18) and (9b) as a function of relative density and the Young modulus is computed using Eq. (19) and the slope of the axial strain/axial stress of unloading of the compaction cycle using the parallelepiped die.

2.4. Wall friction

Friction between powder and tools (die and punch) influences the density distribution of the compact [29,30]. The characterization of die-wall friction coefficient requires measurements of radial stress and transmitted stress to the lower punch. Different equations to compute die-wall friction coefficient exist. However, the main ones used are based on the Janssen-Walker model [31] and on Cedergren's et al. work [32]. Both equations give similar results.

As previously mentioned, the parallelepiped die was not instrumented to measure radial stress and transmitted stress to lower punch. In this study, die-wall friction coefficient was determined from measurements of the compression using the instrumented cylindrical die.

Based on this and using the equation proposed in [32], the wall friction coefficient was then determined as a function of normal pressure, σ_r using Eq. (20).

$$\mu = \frac{(\sigma_z - \sigma_l)\pi R^2}{2\pi RH\sigma_r} \tag{20}$$

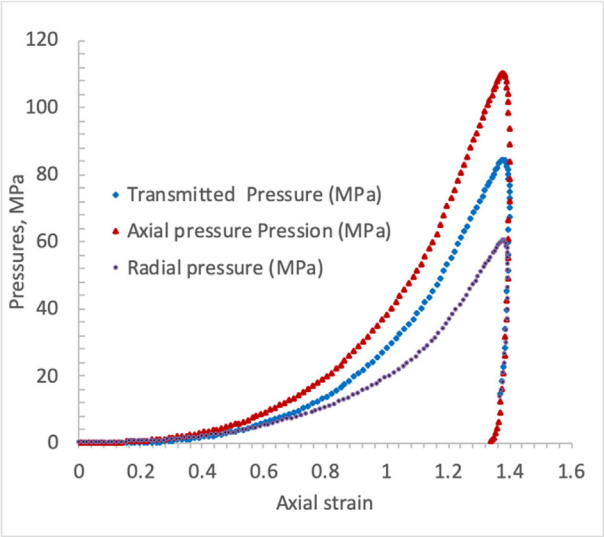

Fig. 4. Compaction cycle of MCC using instrumented cylindrical die.

Where: $R = D/2$, is the internal radius of the die and H is the compact height, $(\sigma_z - \sigma_l)\pi R^2$ and $2\pi RH\sigma_r$ are the mean tangential force and the mean normal force to the cylindrical die wall respectively.

3. Results

3.1. Material parameters of MCC vivapur® 102

In this work, a microcrystalline cellulose powder (vivapur® 102, from J.S. Retenmaïer) was used as model material for the calibration parameters of the DPC model, elastic properties and wall friction coefficient. These parameters were calibrated using the hybrid procedure described in Section 2. The basic characteristics of the powder are summarized in Table 1 [33]. The particle size was measured by Laser diffraction using a Mastersizer 2000 (Malvern Instruments, UK). The bulk density was determined from the measurement of a powder mass and a known volume of powder using a measuring cell. The true density was determined by using a helium pycnometer (AccuPyc 1330, Micromeritics Instrument Corp., USA).

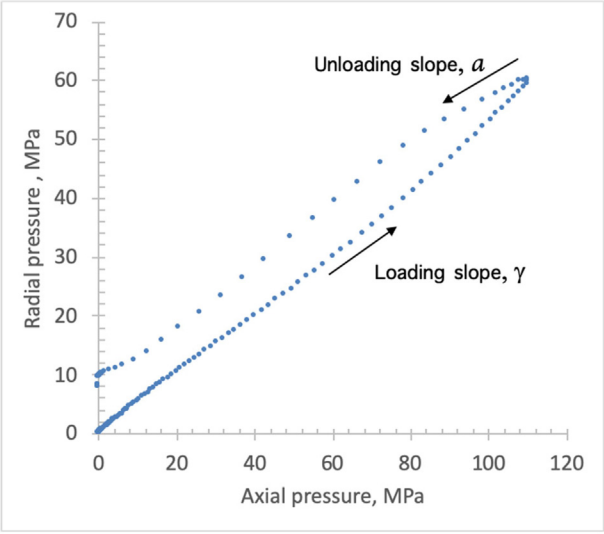

Fig. 5. Radial stress versus axial stress of loading unloading. γ is the slope of the loading and a is the slope of the unloading.

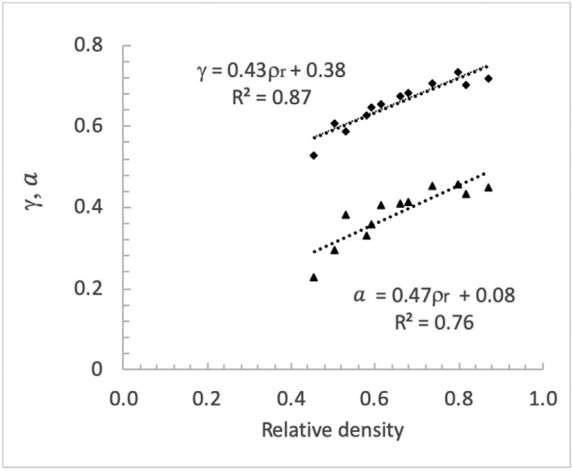

Fig. 6. Radial stress to axial stress ratio, γ (loading) and a (unloading) versus relative density.

3.2. Axial stress/radial stress of loading unloading

A cylindrical die of 1cm^3 of volume (11.28 mm in diameter and 10 mm in height), instrumented to measure radial stress [25] was used to determine γ and a (Eq. (9)) from the axial stress/radial stress of the compaction of MCC. A typical compaction cycle of MCC vivapur® 102 at 110 MPa, is plotted in Fig. 4, showing the pressure on the upper and lower punch and radial stress. The axial stress/radial stress during the loading-unloading is shown in Fig. 5.

The slopes $\gamma = \frac{d\sigma_r}{d\sigma_z}$ (loading) and $a = \frac{d\sigma_r}{d\sigma_z}$ (unloading) were determined for compacts manufactured with relative density in the range 0.42–0.84. Before each compaction, the die-wall was manually lubricated with magnesium stearate. Results of γ and a are plotted in Fig. 6 and a linear fit was considered (Eqs. (21) and (22)) with a confidence of 87% and 76% respectively.

$$\gamma(\rho_r) = 0.43\,\rho_r + 0.38 \tag{21}$$

$$a(\rho_r) = 0.47\,\rho_r + 0.08 \tag{22}$$

Fig. 7 shows the wall friction coefficient of the compaction without die lubrication using Eq. (16). Its variation with normal stress, σ_r shows a mean value of ca. 0.35 which is in agreement with the data obtained in [5,7] for similar material behaviour (Avicel PH102).

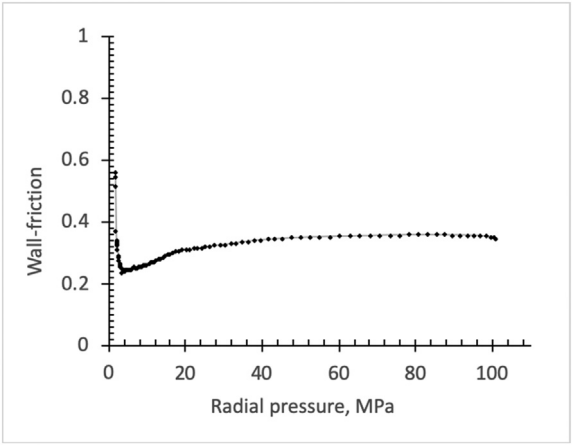

Fig. 7. Die wall friction coefficient versus normal stress (cylindrical die).

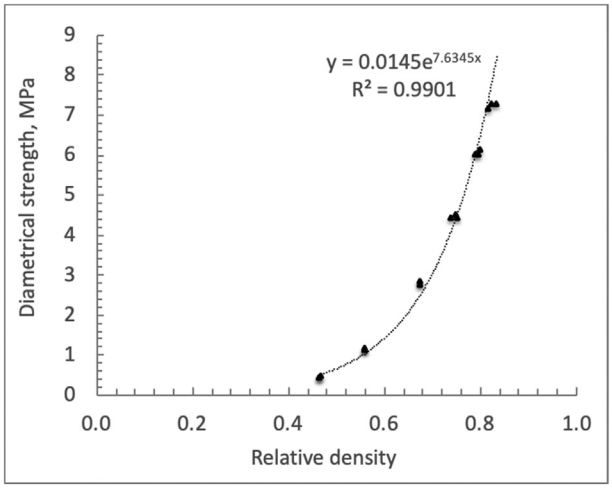

Fig. 8. Diametrical strength vs relative density.

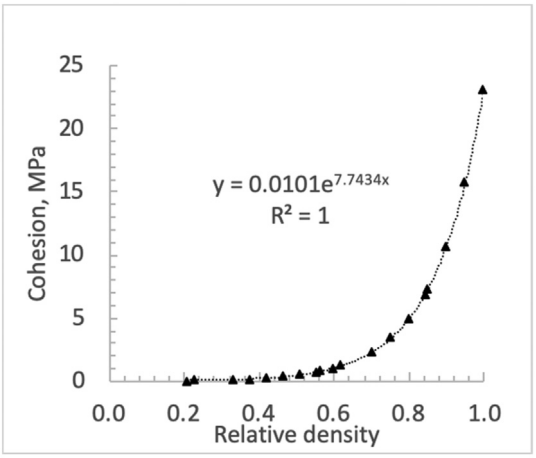

Fig. 10. Computed material cohesion vs relative density (Eq. (16)).

3.3. Cohesion and internal friction angle

Results of the diametrical and axial strength (Eqs. (14) and (15)) are plotted in Figs. 8, 9 according to the relative density. The data were fitted using exponential equations shown in the same figures. The cohesion, d and internal friction angle, β were then computed using Eqs. (16) and (17) using the fitted equations. The evolution plotted in Figs. 10, 11 shows agreements with the data obtanined in [8] for MCC Avicel PH 101 and in [14] for MCC Avicel PH 200.

3.4. Hardening and cap surface parameters

A parallelepiped die volume of 33.7 cm^3 (Lx = 1.56 cm, Ly = 5.4 cm, Lz = 4.0 cm) was used for the compaction of flat and grooved compacts. The system is composed of a fixed lower punch, a movable upper punch and a guiding system to align the active punch with the die. The set was fixed to an Instron uniaxial press equipped with a load sensor of 30 kN (Fig. 1a). The grooved punch and its geometrical surface characteristics are shown in Fig. 1b and 2.

Using the parallelepiped die and two flat punches, the MCC powder was compacted at different load forces (5–30 kN). The die and punches were manually lubricated using magnesium stearate. Compaction cycles at different relative density are shown in Fig. 12. The compacts' properties are listed in Table 2 showing the characteristics of the compacted samples. The relative density variation (expansion) after ejection is also included in the table and is lower than 8%.

As previously mentioned, the parallelepiped die was not instrumented and the ratio of radial stress to axial stress, γ (Eq. (17)) was used. Based on this, hydrostatic pressure, p and Von-Mises stress, q was then calculated using Eqs. (12) and (13) and the axial compaction pressure shown in Table 2. Then, the hydrostatic pressure p_a, the eccentricity R, and the hardening yield function p_b, were computed using Eqs. (6), (7) and (8) respectively. Results of p_a and R are plotted in Figs. 13 and 14 and the evolution of p_b versus plastic volumetric strain, ε_{vol}^{pl} is represented in Fig. 15. Similar results of the eccentricity were obtained in [8]. However, comparatively to the data of the literature [5,8,14], a scale effect due to the compact size can be observed for p_a and p_b. Indeed, due to the punch surface size and the powder bed height, in this study, the applied pressure was in the range 5–35 MPa and the volumetric plastic strain in the range 0.69–1.2, whereas for a punch of 1cm^2 of surface and a powder bed of 10 mm of height, the pressure would vary between 50 and 300 MPa and plastic volumetric strain between 1.1 and 2. This is probably one reason explaining why FEM simulations of compaction are often performed with the same geometry and size to the used die for DPC parameters' calibration.

3.5. Elastic properties

Using Eq. (18), the Poisson ratio was computed from the constant $a = \frac{d\sigma_r}{d\sigma_z}$ in the range 0.42–0.84 of relative density. The results of Poisson

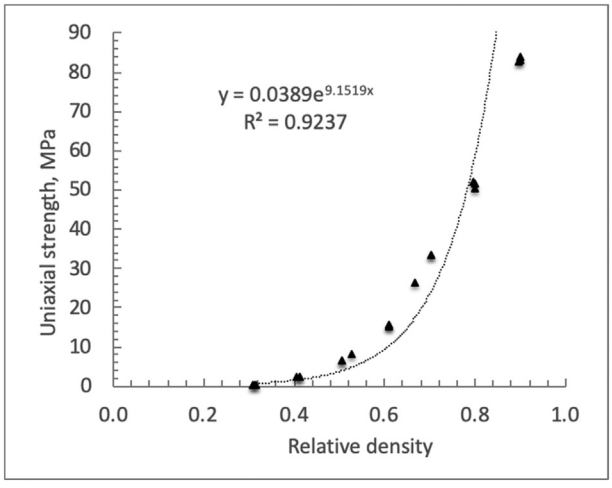

Fig. 9. Uniaxial strength vs relative density.

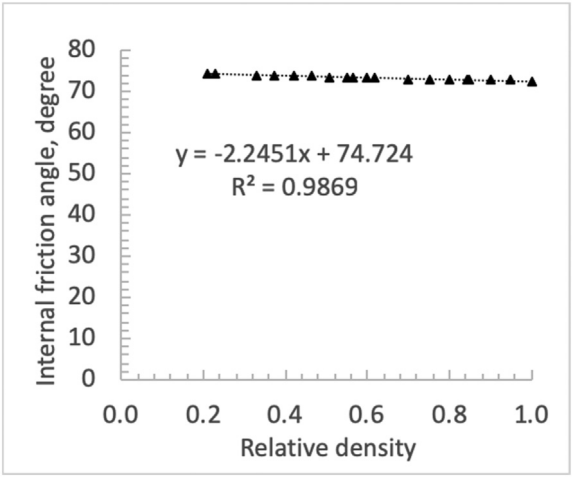

Fig. 11. Computed internal friction angle vs relative density (Eq. (17)).

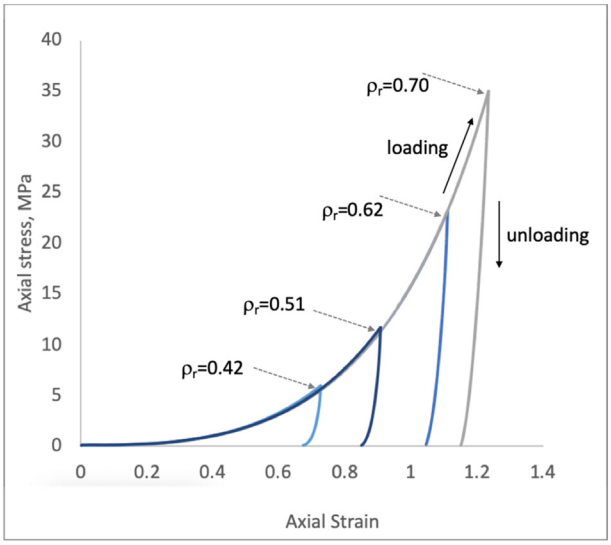

Fig. 12. Compaction cycles of MCC using lubricated parallelepiped die and flat punches.

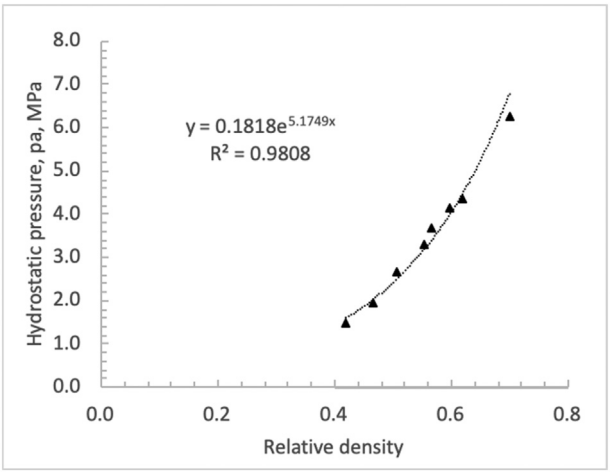

Fig. 13. Hydrostatic pressure, p_a vs relative density.

ratio which are plotted in Fig. 16, are in the range 0.19–0.34. Then, using the Eq. (19), the Young modulus was computed from the determined Poisson ratio and the slope $\frac{d\sigma_z}{d\varepsilon_z}$ of the unloading curve (ε_z, σ_z) shown in Fig. 17. The resulting Young modulus is plotted in Fig. 18 according to the relative density and was fitted using the equation $E = 0.23e^{2.55\rho_r}$ with 96% of confidence. The Poisson ratio varied similarly to other microcrystalline cellulose data published in the literature, whereas the Young modulus peaked at 3 GPa for a full dense material, which was lower in comparison to published data [5,8,14]. This may also be a scale effect as the Young modulus is measured from stress and strain.

Based on the above hybrid procedure of DPC parameters calibration and elastic properties, the obtained data have to be validated. For this, FEM simulations, using ALE Adaptive meshing (Section 4), of the compaction in the parallelepiped die using flat punches were performed and the predicted compaction force and mean relative density were compared to the measurements. Results of the DPC parameters validation are presented in Section 4. Then, simulations of loading and unloading compaction using grooved punches were developed using the validated DPC parameters. The predicted results of relative density are compared to the density distribution resulting from the X-ray microtomography analysis, described below.

3.6. X-ray microtomography characterization of grooved compact

The X-ray microtomography (XRμCT) characterization technic is based on the measurement of the energy attenuation, which is proportionally related to the density [34]. This technic was used to characterize the density distribution of a parallelepiped grooved compact of MCC manufactured at 20kN without die lubrication (Fig. 19). The scan was performed in the central part of the compact along the "y" axis, representing a volume of 2.68 cm^3 ($1.56 \times 1.40 \times 1.34$ cm^3). XRμCT measurements were carried out using an Easytom 130 tomograph with an acceleration voltage of 60 kV and an intensity of 133 μA. The resulting spatial resolution was 17.1 μm. The transmitted X-rays were recorded for 1440 projections per 360° rotation. These images were collected to reconstruct the 3D greyscale image of the compact. Image processing was carried out using the open source software ImageJ [35].

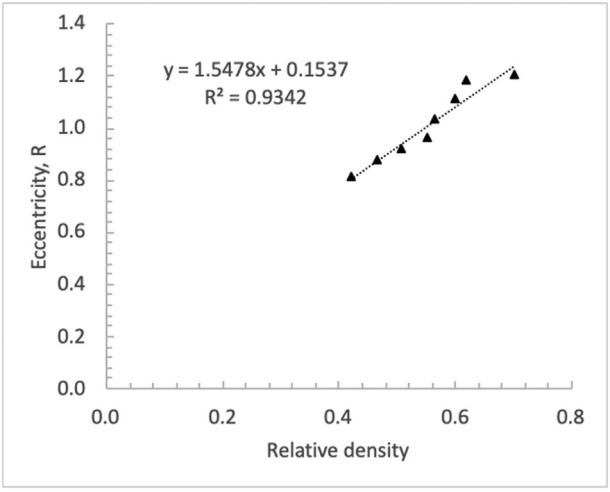

Fig. 14. Eccentricity, R vs relative density.

Table 2
Compaction data of MCC in parallelepiped die and flat punches.

Load (kN)	Pressure (MPa)	Mass (g)	Compact height (mm)	Plastic volumetric strain	Relative density in die, "ρ_r,in" (g/cm^3)	Relative density out of die "ρ_r,out" (g/cm^3)	Expansion (ρ_r,in-ρ_r,out)/ ρ_r,initial	Compact width, x (mm)	Compact depth, y (mm)
5	5.84	10.45	19.4	0.69	0.420	0.398	0.06	15.79	54.26
7	8.17	10.44	17.53	0.79	0.465	0.440	0.06	15.80	54.30
10	11.67	10.42	16.06	0.88	0.508	0.479	0.06	15.80	54.27
13	15.17	10.43	15.01	0.97	0.553	0.514	0.08	15.80	54.28
15	17.51	10.46	14.57	0.99	0.565	0.530	0.07	15.81	54.30
18	21.01	10.43	13.77	1.05	0.598	0.560	0.07	15.79	54.25
20	23.34	10.50	13.38	1.08	0.620	0.580	0.07	15.75	54.28
30	35.02	10.46	11.98	1.20	0.700	0.650	0.08	15.78	54.26

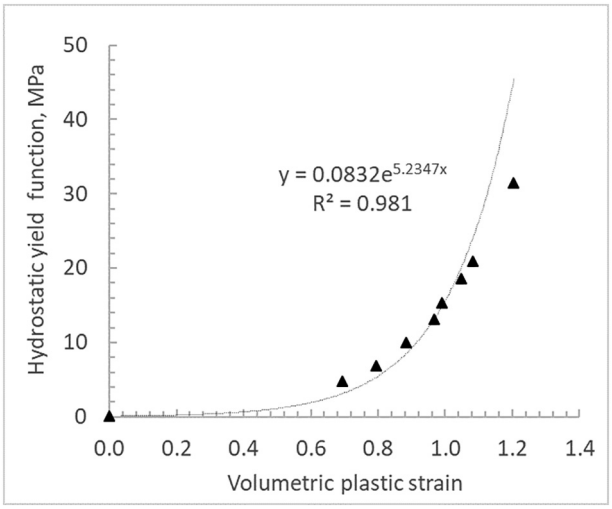

Fig. 15. Hydrostatic yield function, p_b vs plastic volumetric strain, ε_{vol}^{pl}.

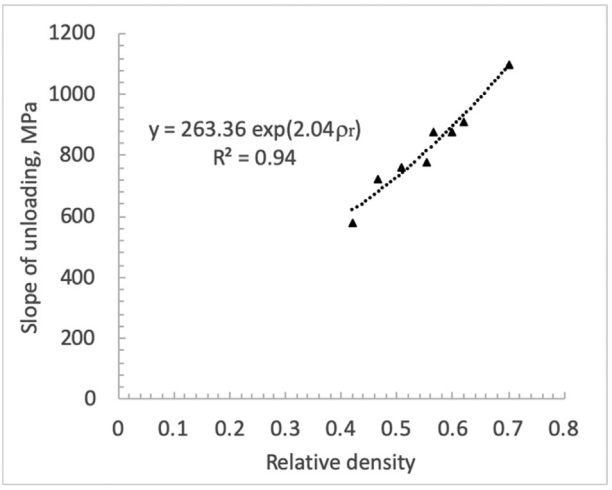

Fig. 17. $\frac{d\sigma_z}{d\varepsilon_z}$ vs relative density (parallelepiped die).

To map the relative density distribution of the X-ray tomography image of the grooved compact, a calibration method correlating grey level values (ranging from 0 to 255) to relative density of cylindrical compacts was used [36–38]. The section below, details the used procedure.

3.7. Relative density calibration

For a better homogeneity of compact density, MCC powder was mixed with 0.5% *w*/w of magnesium stearate in a Turbula mixer (type T2F Willy A. Bachofen, Basel, Switzerland) at 50 rpm for 5 min. Then, eight cylindrical compacts of 0.343 ± 0.004 g of mass and 11.28 mm of diameter were manufactured at different compaction pressures ranging from 7 MPa to 171 MPa using a uniaxial press (Frogerais® OA, France). The density of each compact was calculated from the mass and volume after ejection and ranged from 0.43 to 0.87. X-ray tomography images of the compacts were generated by the Easytom 130 tomograph using the same parameters as for the grooved compact experiment. For each compact, the mean grey level value was computed for 50 slices along the thickness in the central part of the sample. To reduce the wall friction effect, a circular section of 11 mm of diameter was considered for each slice. The averaged grey level value of all the slices representing an equivalent analysed volume of 80.76 mm^3, was computed. A calibration curve correlating the grey level value to relative density of the compact is plotted in Fig. 20 and fitted using a linear equation:

$$GL = 173.57\rho_r + 82.428 \quad (23)$$

Where: GL represents the grey level value.

To map the relative density of the grooved compact using the X-ray tomography image, the Eq. (23) will be used.

3.8. Mapped relative density distribution of the grooved compact

Using the X-ray tomography image of the grooved compact shown in Fig. 19, the density distribution was generated on a 2D section (x,z) in the middle of the compact along the "y" axis. Each pixel grey level was associated to a relative density using Eq. (23). The resulting relative density distribution is plotted in Fig. 21. Other 2D slices located on either side of the middle plane and far from the ends showed similar distributions, indicating a uniform density with respect to the variable y. As the finite element simulation was performed on a 2D plane (x,z) assuming plane strain hypothesis, the comparison between predictions and measurements were made in 2D.

It can be observed, in Fig. 21, that the density distribution is high at the base of the grooves (0.72 under the upper groove and 0.68 above

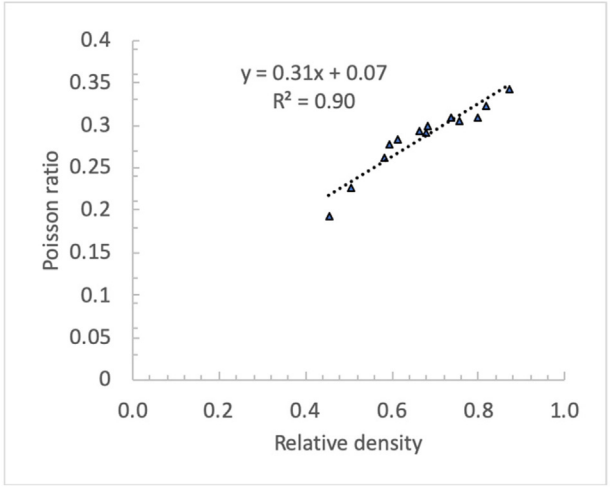

Fig. 16. Poisson ratio versus relative density (cylindrical die).

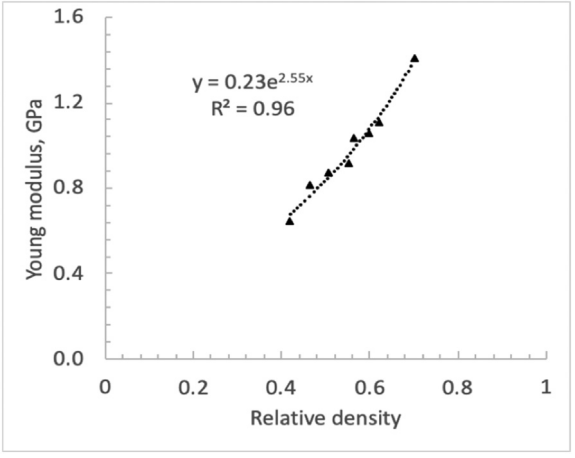

Fig. 18. Young modulus against relative density (computed from Poisson ratio and $\frac{d\sigma_z}{d\varepsilon_z}$).

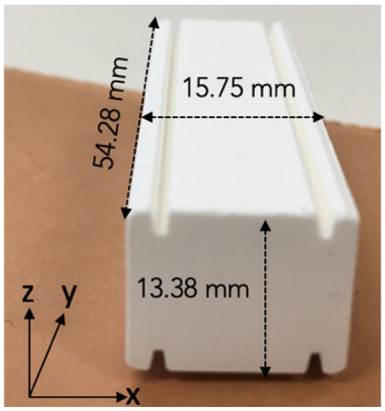

Fig. 19. Grooved compact manufactured at 20 kN with unlubricated die (mean relative density = 0.58).

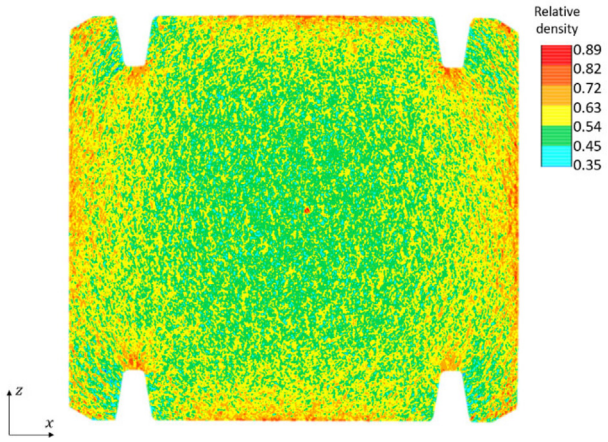

Fig. 21. Density distribution on a slice of the grooved specimen compacted at 20kN (slice in the middle of the compact along y axis) at pixel scale.

the lower). At the powder-punch and powder-die contacts, the densities register slightly lower values (0.618–0.622). The central part of the compact shows a large homogeneous area with intermediate values of relative density of 0.55 on average. However, the lowest values are localized at the shoulders of the grooves (0.49–0.55). This behavioural result is a consequence of the complex flow around a steep singularity, which leads to a weak powder filling. The obtained results present similar tendencies as in [9,14], particularly around the embossed part of the punch. However, as the grooves are located, in this case study, close to the die (instead of the centre of the compact as in [9,14]) with the presence of chamfers, the resulted relative density is not symmetrical on either side of the groove either at the top or the bottom of the compact.

4. Finite element method for compaction simulation

4.1. Description of the simulation procedure using ALE adaptive meshing

The Finite Element Method using Lagrangian approach is largely used for simulation of die compaction [1–13]. In this approach, in which elements are always full of a material, the mesh moves and distorts with the physical material and deform as the material deforms. This solution is particularly suitable for solid-mechanics analysis. However, large deformations may lead to non-conforming elements due to large distortions. This approach is implemented in Abaqus/standard using implicit analysis, which leads to an accurate solution but with a large computational cost per increment. In order to reduce mesh distortion and thus maintain a high-quality mesh, even under severe deformations, [9,39] used a "mesh to mesh solution mapping". This solution consists of results transfer to manually created new mesh between steps through a restart instruction. However, this procedure is time consuming and the transfer of solutions may introduce artificial diffusion, causing loss of accuracy.

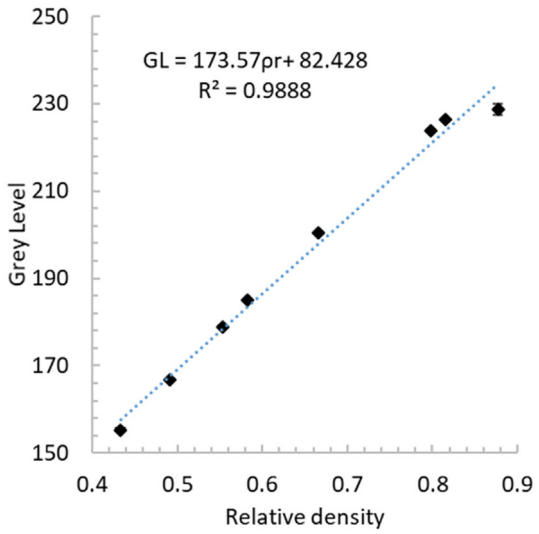

Fig. 20. Grey level, GL vs relative density, ρ_r.

By contrast, in FE simulations using the Eulerian approach, the nodes are fixed in space involving a control volume and the material flows through the elements that do not deform. The advantage of the Eulerian formulation is that no element distortions occur. This method is suitable for fluid mechanics.

To capture the advantages of Lagrangian and Eulerian approaches, Arbitrary Lagrangian Eulerian (ALE) method is implemented in Abaqus/Explicit. In this approach, the finite element mesh is neither attached to the material nor fixed in space. The mesh, in general, has a motion that is independent of the material. This approach was used in [14] for simulating the formation of debossed features, in [40] for metal cutting process and in the main simulations of rolling compaction processes [16–20]. As for the Lagrangian method, large mesh distortions and contact problems can occur due to the large deformations so that a convergent solution cannot be achieved. To reduce mesh distortion, an adaptive meshing procedure is proposed in Abaqus/Explicit during the step. Some options have to be determined to ensure a convergent solution, particularly, the remeshing frequency and the sweep, which define the maximum number of remeshing in a step. The advantage of this procedure is that the adapted mesh is generated by Abaqus and the data transfer between the degenerated mesh and the created mesh is also performed in Abaqus, which reduces the intervention time of the user.

In this study, finite element simulation of the compaction was performed using the Arbitrary Lagrangian-Eulerian approach (ALE) implemented in Abaqus/Explicit v6.18. Details on the main data of the simulation are given below.

All the parameters of DPC for MCC powder were expressed as functions of the relative density and included in the input file. The computation of the relative density from the plastic volumetric strain was implemented into a user subroutine VUSDFLD in Abaqus/Explicit.

Simulations of the compaction were conducted using firstly the parallelepiped die and flat punches for the validation of DPC parameters. The validated parameters were then used for the compaction simulation of the grooved compact. Finally, the predicted and measured relative density using X-ray tomography (Fig. 21) were compared. In the simulations, the punches and die were considered as rigid bodies. The initial volume of the powder was of $1.56 \times 5.4 \times 4.0$ cm^3. The resulting initial

relative density was of 0.195 (relative density of loose powder). Due to the large dimension of the compact in the "y" axis, the dependency of the displacement field on the "y" coordinate is neglected in the main central part (far from the boundary conditions) and the 3D solution was approximated by a 2D solution assuming plane strain conditions in (x,z). A symmetry plane in the "x" direction was also considered to reduce the computation cost. The powder domain was meshed using plane strain element CPE4R with reduced integration. Fig. 22 and Fig. 2 show the meshed part and the grooved punch characteristics respectively. To prevent the element distortions resulting from the large strain, the adaptive meshing algorithm in Abaqus/Explicit was employed. To check and update the mesh, the sweep and the frequency parameters were fixed at 3 and 5 respectively. For the powder-die and powder-punch contact model (contact pair in Abaqus/Explicit), the kinematic contact algorithm proposed in Abaqus was considered for the mechanical constraint. The friction coefficient was 0. for the compaction with the flat punches (validation of DPC parameters and elastic properties) and 0.35 for the compaction with the grooved punches. For both simulations using flat and grooved punches, the powder compaction was made by moving the upper punch downward in the z direction using the same maximal displacement as in the experiments and by removing it upward to simulate the loading and unloading. Due to numerical convergence difficulties, the ejection did not totally succeed. As simulation results are mesh-dependent, various simulations were performed by increasing the number of elements (12194, 19152, 25283, 34048). The evolution of maximum and minimum relative density, as well as the minimum and maximum hydrostatic pressure, are summarized in Table 3, showing a stable solution with respect to the used mesh. The presented results were obtained using 19125 elements.

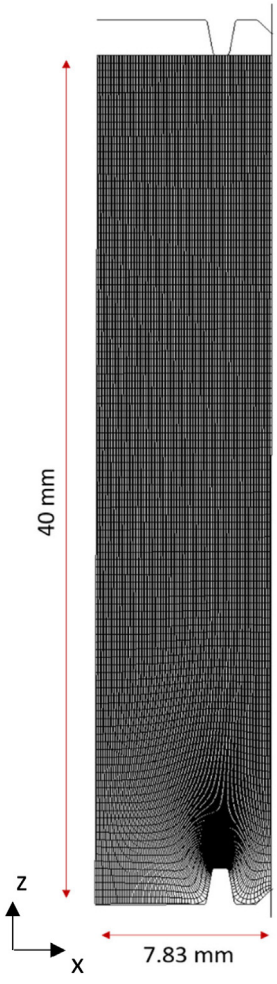

Fig. 22. Initial mesh.

Table 3
Minimal, maximal relative density and hydrostatic pressure: sensitivity to mesh refinement.

Number of elements	Minimal relative density	Maximal relative density	Minimal pressure (MPa)	Maximal pressure (MPa)
12,194	0.4279	0.7750	0.815	24.70
19,152	0.4199	0.7631	0.685	25.27
25,283	0.3933	0.7405	0.559	25.71
34,048	0.4268	0.7482	0.896	26.79

4.2. Validation of DPC parameters

To validate the DPC parameters and elastic properties, simulations of loading and unloading were conducted using the parallelepiped die and the flat punches without friction. The predicted "axial displacement-compaction force cycles" for 10kN, 20kN and 30kN are superimposed to the experimental cycles in Fig. 23. The mean squared error calculated between experimental and numerical results is of 0.092 and the standard deviation of 0.303. As it can be seen in Fig. 23, predictions are in good agreements with the experiments, confirming that the explicit integration method using ALE adaptive meshing procedure allowed to obtain a good prediction of the compaction force. Moreover, for the 20kN compacted sample, the predicted relative density varied in the range (0.604–0.616), presenting a spread of 1.9%. The computed average relative density (0.612) presented a relative deviation of 5% compared to the measured average relative density (0.58) after ejection of the compact. This deviation is acceptable in regard to the lack of ejection simulation.

4.3. Simulation results using grooved punches

As mentioned previously loading and unloading simulations using grooved punches were performed using constant die wall friction ($\mu = 0.35$). The axial upper punch displacement was as in the compaction experiment for 20 kN.

In Fig. 24 (resp. Fig. 25) the isovalues of axial displacement (resp. radial displacement) after unloading are plotted. The axial displacement shows deformed bands under the compaction and the impact on their shapes resulted from the indentation of the powder by the punch groove. The radial displacement provides information on the powder

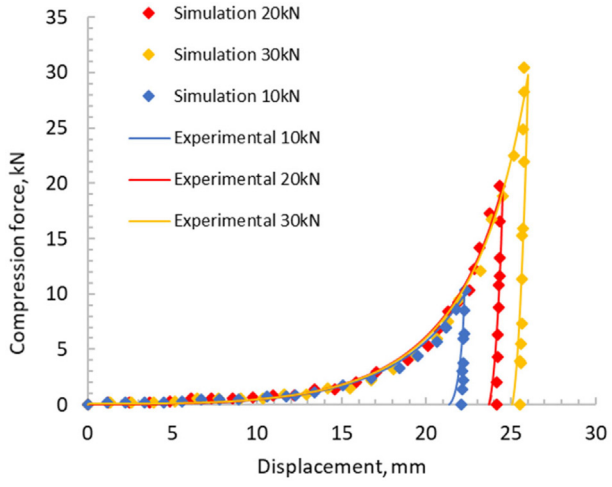

Fig. 23. Comparison of numerical and experimental compaction cycle (average relative density $\rho_r = 0.68$ at 30kN, $\rho_r = 0.61$ at 20kN and $\rho_r = 0.53$ at 10kN).

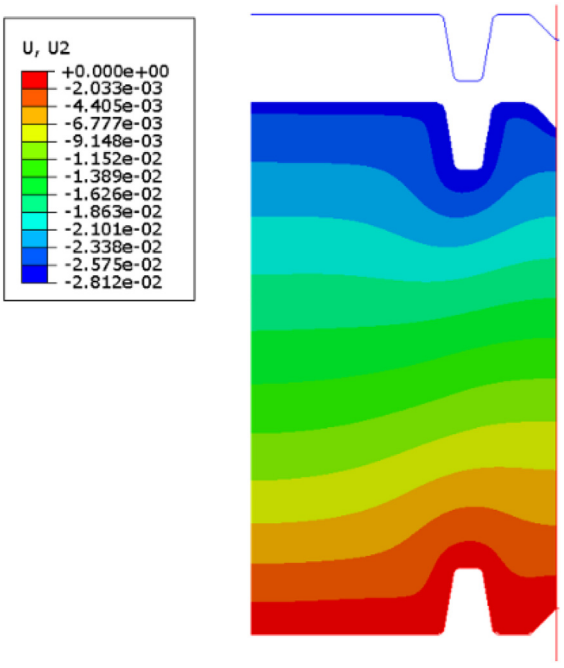

Fig. 24. Displacement along z axis [m] (unloading).

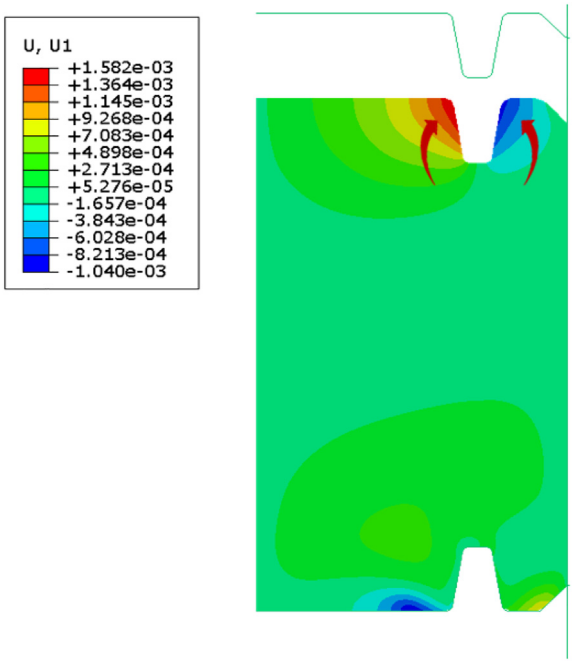

Fig. 25. Displacement along x axis [m] (unloading).

flow into the vicinity of the upper groove. In fact, when the upper punch groove indented the material, the powder is forced to flow into either side of the groove, which lead to a complex powder flow into the dead zones under the groove shoulders.

The results of Von-Mises stress and relative density distributions for loading and unloading are plotted in Fig. 26 and Fig. 27 respectively.

For the loading step, Von-Mises stress distributions varied from 1.68 to 51.27 MPa showing high values under the upper groove (47.1–51.3 MPa) and relatively lower ones on the top of the bottom groove (30.6–34.7 MPa). Low shear stresses are obtained in the central part of the compact and on either side of the groove flanks and shoulders (1.6–9.9 MPa). Overall, the steep shape of the groove, its location near the die, and the presence of chamfer results in a complex shear gradient field in the vicinity of the grooves. In order to reduce the shear gradient in this zone, an optimization of the groove's shape and spatial position respecting the end use of the product, constitutes a future challenge.

The elastic recovery after the unloading (Fig. 26) leads to a stress redistribution in the sample with a decrease of the shear stress in the vicinity of the grooves. There is also no shear field symmetry on either side of the groove.

Regarding the relative density distribution (Fig. 27), results show the highest values under the upper groove (0.73–0.76) and the lowest ones in the area between the die and the lower groove flank (0.42–0.5). A large part, which extends from the compact centre to the die has a homogeneous relative density with a mean value of 0.58. The main relative density gradient is localized between the grooves, in the vicinity of the grooves and in the closed area between the grooves and the chamfers. Similar to the shear stress, a low relative density is predicted on the flanks and the shoulders of the grooves, showing the complex powder flow around the groove leading to a weak filling of the shoulders. As can be seen, a poor drop of density was observed during the unloading phase as the relative density is computed from the plastic volumetric strain (user subroutine VUSDFLD), which underwent a small variation during the unloading.

4.4. Comparison with the literature

Comparison to existing numerical works in the literature is always a tedious matter due to differences in geometry, numerical methods, model parameters, friction conditions or the boundary conditions that might influence the comparison. We preferred focalizing the comparison on the global tendencies of the material flow around the geometrical singularity of the active punch surface such as the grooves used in this work, a debossed feature in [14] or a cylindrical protrusion in [9]. As previously presented, the predictions showed results of high and localized relative densities under the groove with a rapid decay away from it, and lower densities at the shoulders. Similar tendencies were also obtained in modelling the formation of debossed features of pharmaceutical tablets [14]. In that work, the embossed part, having a shape close to that of a sphere, was at the centre of the cylindrical tablet, far from the die and without a chamfer that strongly influenced the material flow in the vicinity. Other differences concerned the design of the groove such as the stroke angle, which was fixed in this study to 10° (>25° in [14]) leading to a dead area at the shoulders of the groove, less accessible to powder filling. Results found in [9] also presented similarities to the present work, in particular for the density distribution in the vicinity of the protrusion where the density was higher at the top of the protrusion and lower on the flanks. In this work, the protrusion concerned the lower punch, which was positioned at the compact centre and the active punch was flat. However, the stroke angle could be considered as 0° which accentuates the difference of the density at the top of the protrusion and on the flanks. Another detail concerns the numerical method that can influence the results. Indeed, in [9], the authors performed an implicit discretization of the boundary problem using Abaqus/Standard and a 'mesh-to-mesh solution mapping' to update distorted meshes, while in [14], an explicit procedure in Abaqus/Explicit was used with an adaptive meshing algorithm to allow the elements to conform to large deformations. This method seems to be similar to the ALE approach used in our study, but few details were given for a deeper comparison.

4.5. Confrontation of FEM predictions and X-ray microtomography measurements

For the comparison between FEM prediction and XRμCT measurements, regions of interest in the surrounding of the upper and lower

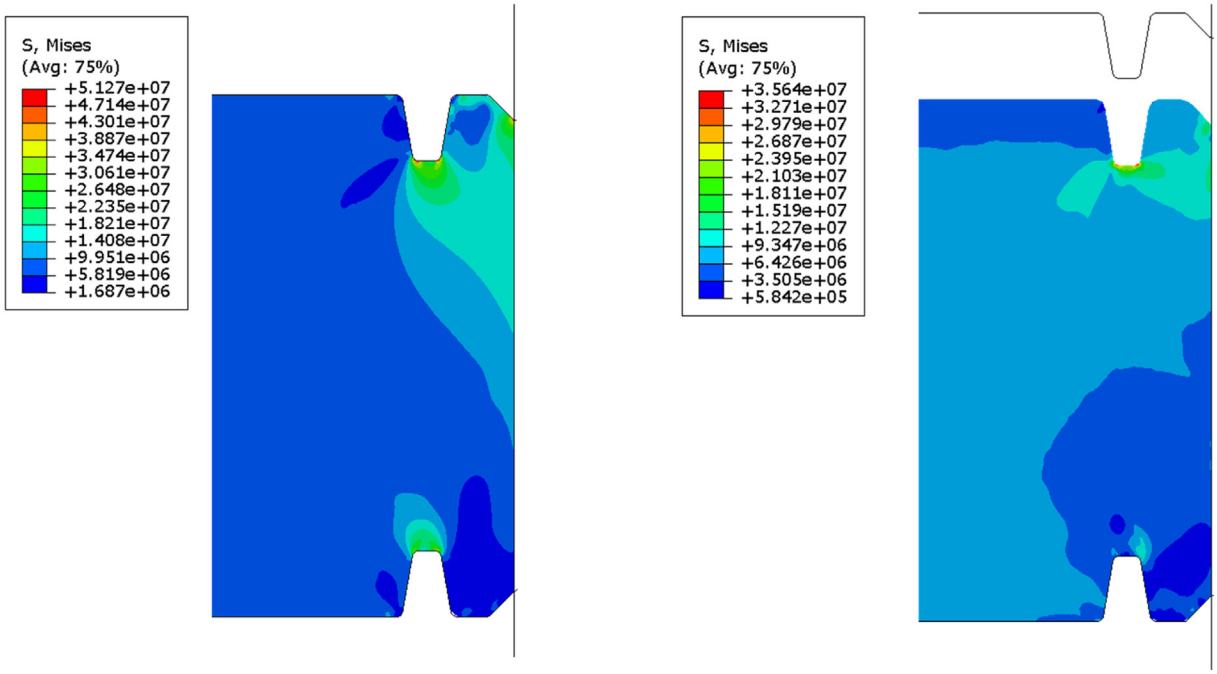

Fig. 26. Von Mises stress [Pa] distribution for loading (left) and unloading (right).

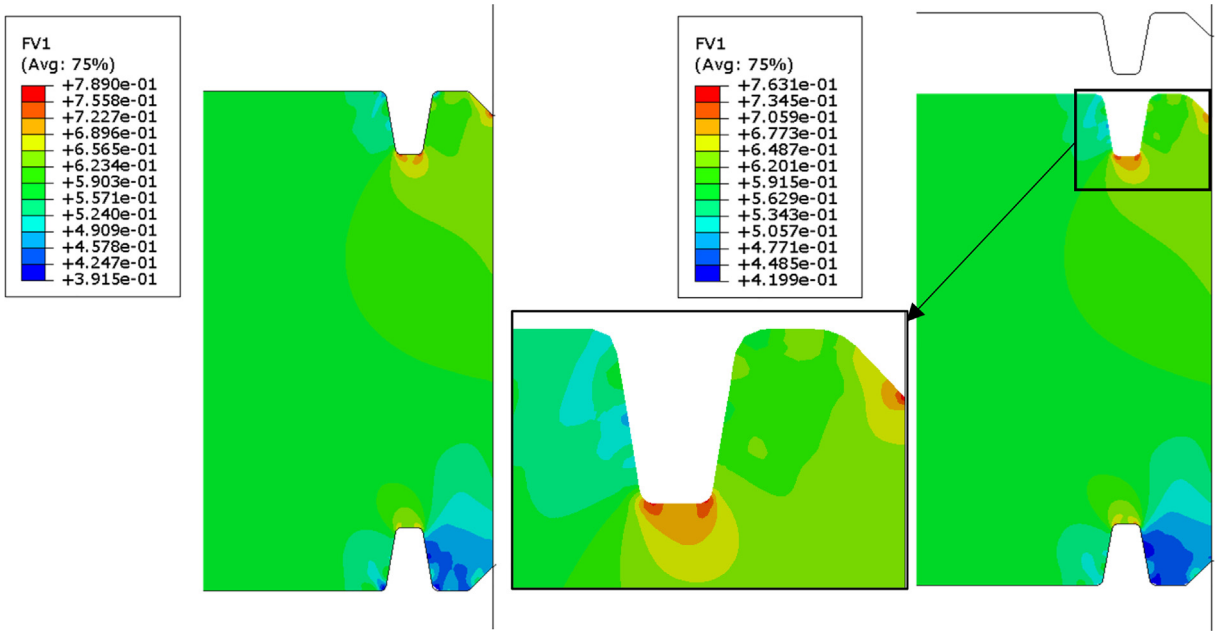

Fig. 27. Relative density distribution after loading (left) and unloading (right).

punch and in the centre of the compact are defined and shown in Fig. 28. For X-ray measurements, relative density values were computed for each region corresponding to 10×10 pixels equivalent to a surface of 170 μm × 170 μm. This surface corresponded to approximately $6 \times 3 = 18$ finite elements on which the predicted relative density was averaged. Table 4 displays results of relative density measured using X-ray tomography and predicted by FEM simulations.

Results in Table 4 show a good agreement between FEM predictions and tomography results. However, for regions in the upper and lower edges (zones 6,7 and 13,14), a deviation is to be noted, varying between 4.6% and 7.7%.

Another zone located between the two facing grooves is also of high interest because it concentrates the main variations of density and undergoes tension in the unloading step, which can lead to damage initiation. Accurate predictions of relative density in this zone can help, for future work, to optimize the groove's shape by decreasing the intensity of the density gradient. The predictions and measurements of relative density along z axis between the faced grooves are plotted in Fig. 29. The plot showed a density gradient for both the measurements and the predictions with high densities at the grooves and lower densities in the middle. A relative difference of the density between the middle and the groove base of 23.6% was estimated. As can be seen in Fig. 29,

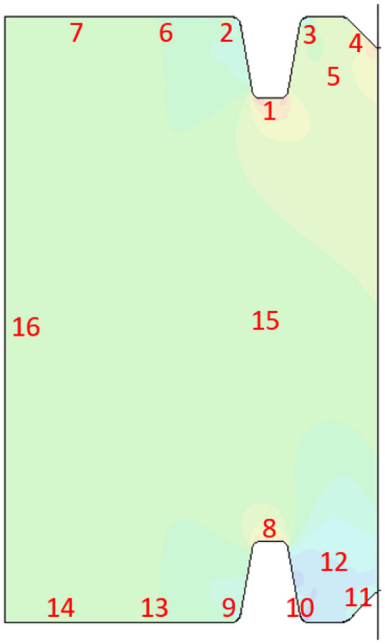

Fig. 28. Zones localization (numbers in Table 4) for relative density confrontation of FEM predictions and X-ray tomography results.

Table 4
Relative density values for numerical prediction and X-ray tomography results. (averages in the different zones defined in Fig. 28).

Zone	X ray tomography – relative density	FEM simulation – relative density	Relative deviation (%)
1	0.725	0.712	1.79
2	0.537	0.534	0.55
3	0.595	0.596	0.16
4	0.684	0.665	2.77
5	0.602	0.610	1.32
6	0.609	0.576	5.41
7	0.622	0.577	7.70
8	0.684	0.672	1.75
9	0.522	0.526	0.76
10	0.501	0.487	2.79
11	0.524	0.507	3.24
12	0.493	0.487	1.21
13	0.609	0.580	4.76
14	0.618	0.589	4.69
15	0.591	0.598	1.18
16	0.556	0.577	3.77

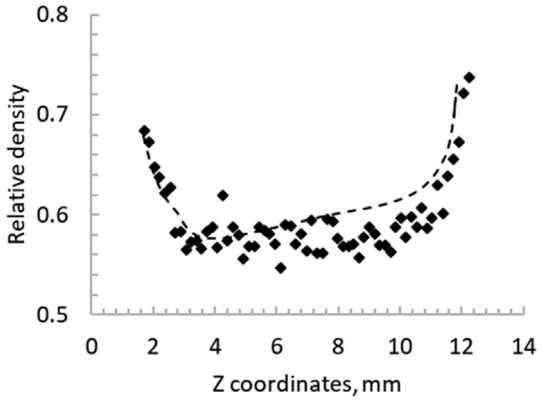

Fig. 29. Comparison of relative density distribution along z axis between two facing grooves.

FEM predictions and measurements of the relative density are in good agreement. The mean squared error calculated between experimental and numerical results is of 0.00066 and the standard deviation of 0.0257.

5. Conclusion

This work presents an FEM modelling for predicting density distribution in the vicinity of two facing grooves and in between, on a parallelepiped compact with validation of the results using X-ray tomography analysis.

An experimental hybrid procedure for the identification of DPC parameters and elastic properties powder is described. The hybrid procedure combines measurements from instrumented cylindrical die with radial stress, and compaction cycles of flat parallelepiped compacts. The obtained properties were numerically validated and then were used to investigate the development of stress and relative density fields in the grooved parallelepiped compact. FEM simulations of loading and unloading were performed using the Arbitrary Lagrangian Eulerian method (ALE) developed in Abaqus/Explicit. As the DPC material parameters are density-dependent, a user subroutine was developed. Furthermore, as simulation results are mesh-dependent, optimized meshes were sought for a stable solution.

Results of the compaction simulation showed a good agreement between the measured and predicted densities particularly in the vicinity of the grooves. Analysis of the measured and predicted density distribution showed a large variation between the two facing grooves with high values at the grooves and lower values in the middle. The resulting strong density gradient constitutes a fragility in this zone which can lead to cracking under tension during unloading for brittle materials.

More generally, it was shown that the proposed hybrid calibration procedure allowed to access to DPC material parameters and elastic properties for FEM compaction simulation using a large parallelepiped die not benefiting from radial instrumentation. Its use could be extended to other die shapes and sizes by considering radial measurement using an instrumented cylindrical die. Moreover, the explicit method using the ALE approach demonstrated its robustness for solving powder die compaction problems when strong distortions are inevitable using an implicit method.

Declaration of Competing Interest

The authors declare that they have no known competing financial interests or personal relationships that could have appeared to influence the work reported in this paper.

References

[1] P.R. Brewin, O. Coube, P. Doremus, J.H. Tweed, Modelling of Powder Die Compaction, Springer-Verlag London Limited, 2008.
[2] N.P. Lavery, et al., Sensitivity study on powder compaction, AEA Technology Report AEAT-04035, June 1998.
[3] I.M. Cameron, et al., Friction measurement in powder die compaction by shear plate technique, Powder Metall. 45 (2002).
[4] B. Eiliazadeh, B.J. Briscoe, Y. Sheng, K. Pitt, Investigating density distributions for tablets of different geometry during the compaction of pharm, Part. Sci. Technol. 21 (4) (2003) 303–316.
[5] I.C. Sinka, J.C. Cunningham, A. Zavaliangos, The effect of wall friction in the compaction of pharmaceutical tablets with curved faces: a validation study of the Drucker–Prager Cap model, Powder Technol. 133 (1) (2003) 33–43.
[6] A. Djemai, I.C. Sinka, NMR imaging of density distributions in tablets, Int. J. Pharm. 319 (2006) 55–62.
[7] C.-Y. Wu, B.C. Hancock, A. Mills, A.C. Bentham, S.M. Best, J.A. Elliott, Numerical and experimental investigation of capping mechanisms during pharmaceutical tablet compaction, Powder Technol. 181 (2) (2008) 121–129.
[8] L.H. Han, J.A. Elliott, A.C. Bentham, A. Mills, G.E. Amidon, B.C. Hancock, A modified Drucker-Prager Cap model for die compaction simulation of pharmaceutical powders, Int. J. Solids Struct. 45 (2008) 3088–3106.
[9] L. Han, P. Laity, R. Cameron, J. Elliott, Density and plastic strain evaluations using small-angle X-ray scattering and finite element simulations for powder compacts of complex shape, J. Mater. Sci. 46 (18) (2011) 5977–5990.

[10] M.S. Kadiri, A. Michrafy, The effect of punch's shape on die compaction of pharmaceutical powders, Powder Technol. 239 (2013) 467–477.
[11] P.R. Laity, Effects of punches with embossed features on compaction behaviour, Powder Technol. 254 (2014) 373–386.
[12] A. Krok, M. Peciar, R. Fekete, Numerical investigation into the influence of the punch shape on the mechanical behavior of pharmaceutical powders during compaction, Particuology 16 (C) (2014) 116–131.
[13] H. Diarra, V. Mazel, V. Busignies, P. Tchoreloff, Investigating the effect of tablet thickness and punch curvature on density distribution using finite elements method, Int. J. Pharm. 493 (1–2) (2015) 121–128.
[14] S. Swaminathan, J. Hilden, B. Ramey, C. Wassgren, Modeling the formation of debossed features on a pharmaceutical tablet, J. Pharm. Innov. 11 (3) (2016) 214–230.
[15] P. Doremus, Model input data –failure, Modelling of Powder Die Compaction, Springer-Verlag, London 2008, pp. 95–103.
[16] R.T. Dec, A. Zavaliangos, J.C. Cunningham, Comparison of various modeling methods for analysis of powder compaction in roller press, Powder Technol. 130 (2003) 265–271.
[17] J.C. Cunningham, D. Winstead, A. Zavaliangos, Understanding variation in roller compaction through finite element-based process modeling, Comput. Chem. Eng. 34 (2010) 1058–1071.
[18] A. Michrafy, H. Diarra, J.A. Dodds, M. Michrafy, Experimental and numerical analysis of homogeneity over strip width in roll compaction, Powder Technol. 206 (2011) 154–160.
[19] A. Michrafy, H. Diarra, J.A. Dodds, M. Michrafy, L. Penazzi, Analysis of strain stress state in roller compaction process, Powder Technol. 208 (Issue 2) (25 March 2011) 417–422.
[20] Ariel R. Muliadi, James D. Litster, Carl R. Wassgren, Validation of 3-D finite element analysis for predicting the density distribution of roll compacted pharmaceutical powder, Powder Technol. 237 (2013) 386–399.
[21] Abaqus, Abaqus 6.18 Theory Manual, ABAQUS inc, 2018.
[22] F.L. DiMaggio, M. ASCE, I. Sandler, Material model for granular soils, J. Eng. Mech. Div., Proc. Am. Soc. Civ. Eng. (1971) 935–950.
[23] Alon Mazor, Lucia Perez-Gandarillas, Alain de Ryck, Abderrahim Michrafy, Effect of roll compactor sealing system designs: a finite element analysis, Powder Technol. 289 (2016) 21–30.
[24] L. Perez-Gandarillas, A. Mazor, O. Lecoq, A. Michrafy, Compaction properties of dry granulated powders based on Drucker–Prager Cap model, Powder Technol. 337 (2018) 43–50.
[25] A. Michrafy, H. Diarra, J.A. Dodds, Compaction behavior of binary mixtures, Powder Technol. 190 (2009) 146–151.
[26] A. Michrafy, D. Ringenbacher, P. Tchoreloff, Modelling the compaction behaviour of powders: application to pharmaceutical powders, Powder Technol. 127 (2002) 257–266.
[27] I. Aydin, B.J. Briscoe, K.Y. Sanliturk, The internal form of compacted ceramic components: a comparison of a finite element modelling with experiment, Powder Technol. 89 (1996) 239–254.
[28] Baosheng Zhang, Mukesh Jain, Chenghao Zhao, Michael Bruhis, Roger Lawcock, Kevin Ly, Experimental calibration of density-dependent modified Drucker-Prager/cap model using an instrumented cubic die for powder compact, Powder Technol. 204 (2010) 27–41.
[29] M.H. Es-Saheb, Uniaxial strain rate effects in pharmaceutical powders during cold compaction, J. Mater. Sci. 27 (1992) 4151–4159.
[30] B.J. Briscoe, S.L. Rough, The effects of wall friction in powder compaction, Colloids Surf. A Physicochem. Eng. Asp. 137 (1998) 103–116.
[31] R.M. Nedderman, Statics and Kinematics of Granular Materials, Cambridge University Press, 1992.
[32] J. Cedergren, N.J. Sorensen, A. Bergmark, Three-dimensional analysis of compaction of metal powder, Mech. Mater. 34 (5) (2002) 43–59.
[33] A. Michrafy, M. Michrafy, M.S. Kadiri, J.A. Dodds, Predictions of tensile strength of binary tablets using linear and power law mixing rules, Int. J. Pharm. 333 (2007) 118–126.
[34] Steve Burch, Measurement of density variations in compacted parts using X-ray computerised tomography, Metal Powder Rep. 57 (2) (2002) 24–28.
[35] RASBAND, S. Wayne, et al., ImageJ, 1997.
[36] I.C. Sinka, et al., Measurement of density variations in tablets using X-ray computed tomography, Int. J. Pharm. 271 (1–2) (2004) 215–224.
[37] Busignies, Virginie, et al., Quantitative measurements of localized density variations in cylindrical tablets using X-ray microtomography, Eur. J. Pharm. Biopharm. 64.1 (2006) 38–50.
[38] Miguélez-Morán, M. Andres, et al., Characterisation of density distributions in roller-compacted ribbons using micro-indentation and X-ray micro-computed tomography, Eur. J. Pharm. Biopharm. 72.1 (2009) 173–182.
[39] O. Coube, H. Riedel, Numerical simulation of metal powder die compaction with special consideration of craking, Powder Metall. 43 (2) (2000) 123–131.
[40] M. Movahhedy, M.S. Gadala, Y. Altintas, Simulation of the orthogonal metal cutting process using an arbitrary Lagrangian-Eulerian finite-element method, J. Mater. Process. Technol. 103 (2000) 267–275.